

This content has been downloaded from IOPscience. Please scroll down to see the full text.

Download details:

IP Address: 81.158.19.253

This content was downloaded on 26/01/2018 at 07:20

Please note that [terms and conditions apply](#).

You may also be interested in:

[Band parameters of phosphorene](#)

L C Lew Yan Voon, J Wang, Y Zhang et al.

[Focus on silicene and other 2D materials](#)

Motohiko Ezawa and Guy Le Lay

[Interaction of silicene and germanene with non-metallic substrates](#)

M Houssa, E Scalise, B van den Broek et al.

[Selection rule for the optical spectrum of armchair-edge silicene nanoribbons](#)

Hairui Bao, Wenhua Liao, Junji Guo et al.

[Revivals of electron currents and topological-band insulator transitions in 2D gapped Dirac materials](#)

E. Romera, J. C. Bolívar, J. B. Roldán et al.

[Two-dimensional hexagonal tin: ab initio geometry, stability, electronic structure and functionalization](#)

B van den Broek, M Houssa, E Scalise et al.

[Disorder driven transition beyond two-component, single-flavor Dirac physics in silicene](#)

Partha Goswami

[Massive Dirac quasiparticles in the optical absorbance of graphene, silicene, germanene, and tinene](#)

Lars Matthes, Olivia Pulci and Friedhelm Bechstedt

## Theory of Magnetoelectric Properties of 2D Systems

S C Chen, J Y Wu, C Y Lin and M F Lin

---

Chapter 2

## The generalized tight-binding model

To fully understand the electronic properties of emergent layered materials, we propose the generalized tight-binding model to solve the various Hamiltonians under the magnetic and electric fields. The typical systems, graphene, silicene, germanene, tinene, phosphorene and  $\text{MoS}_2$ , are suitable for a model study. The planar/buckled/puckered and layered structures, with the distinct lattice symmetries, layer numbers and stacking configurations, are taken into consideration. Furthermore, the geometry- and atom-dominated interactions, the site energies, the single- or multi-orbital hopping integrals, the orbital-dependent SOC, and the intralayer and interlayer atomic interactions, are included in the Hamiltonian. The field-created independent Hamiltonian matrix elements are derived in the analytic form, especially for the characteristics of this model (reliability, suitability, extension and combination), which are directly reflected in the delicate calculations of magneto-electronic properties, are discussed in detail. How to use it in studying other essential properties is worthy of a closer discussion, such as the combinations with the modified random-phase approximation and the static/dynamic Kubo formula. Finally, the diagonalization of a huge Hermitian matrix can be efficiently done by using the band-like one and the features of the LL spatial distributions.

## 2.1 Monolayer graphene

Monolayer graphene, as shown in figure 1.1(a), has a honeycomb lattice with the C–C bond length  $b = 1.42 \text{ \AA}$ . In the absence of external fields, there are two carbon atoms, the A and B atoms, in a primitive unit cell. The low- and middle-energy essential properties are dominated by the  $2p_z$  orbitals. This indicates that the Bloch wave function is a linear superposition of two tight-binding functions due to the

periodical orbitals.  $|\Psi_{\mathbf{k}}\rangle = c_A|A_{\mathbf{k}}\rangle + c_B|B_{\mathbf{k}}\rangle$ , where  $|A_{\mathbf{k}}\rangle$  and  $|B_{\mathbf{k}}\rangle$ , respectively, stand for the tight-binding functions of the A and B atoms:

$$\begin{aligned} |A_{\mathbf{k}}\rangle &= \frac{1}{\sqrt{N_A}} \sum_{J=1}^{N_A} \exp(i\mathbf{k} \cdot \mathbf{R}_{A_J}) \chi(\mathbf{r} - \mathbf{R}_{A_J}); \\ |B_{\mathbf{k}}\rangle &= \frac{1}{\sqrt{N_B}} \sum_{J=1}^{N_B} \exp(i\mathbf{k} \cdot \mathbf{R}_{B_J}) \chi(\mathbf{r} - \mathbf{R}_{B_J}). \end{aligned} \quad (2.1)$$

$N_A(N_B)$  is the total number of A(B) atoms, and  $\chi(\mathbf{r} - \mathbf{R}_{A_J})$  ( $\chi(\mathbf{r} - \mathbf{R}_{B_J})$ ) is the normalized  $2p_z$  orbital wave function centered at  $\mathbf{R}_{A_J}(\mathbf{R}_{B_J})$ . When the nearest-neighbor atomic interaction (hopping integral  $\gamma_0 = -2.6$  eV [1]) is taken into consideration, it is sufficient in understanding the main features of the  $\pi$ -electronic structure. As a result, the Hamiltonian matrix elements built from the space spanned by the two tight-binding functions are expressed as

$$\begin{aligned} \langle A_{\mathbf{k}}|H|A_{\mathbf{k}}\rangle &= \langle B_{\mathbf{k}}|H|B_{\mathbf{k}}\rangle = 0, \\ \langle A_{\mathbf{k}}|H|B_{\mathbf{k}}\rangle &= \gamma_0(\exp(-ik_x b) + 2 \exp(ik_x b/2) \cos(k_y \sqrt{3} b/2)); \\ \langle B_{\mathbf{k}}|H|A_{\mathbf{k}}\rangle &= \langle A_{\mathbf{k}}|H|B_{\mathbf{k}}\rangle^*. \end{aligned} \quad (2.2)$$

In the presence of a uniform perpendicular magnetic field  $\mathbf{B} = B_z \hat{z}$ , the vector potential, being chosen as  $\mathbf{A}(r) = B_z x \hat{y}$ , can create a position-dependent phase of  $G_n = \frac{2\pi}{\Phi_0} \int_{\mathbf{R}_n}^{\mathbf{r}} \mathbf{A} \cdot d\mathbf{l}$  in the tight-binding functions.  $\Phi_0 = hc/e$  ( $4.1356 \times 10^{-15} [\text{T} \cdot \text{m}^2]$ ) is the flux quantum. The nearest-neighbor hopping integral is modulated as

$$\langle A_{J,\mathbf{k}}|H|B_{I,\mathbf{k}}\rangle = \gamma_0 \exp \left\{ i \left[ \mathbf{k} \cdot (\mathbf{R}_I - \mathbf{R}_J) + \frac{2\pi}{\Phi_0} \int_{\mathbf{R}_{B_I}}^{\mathbf{R}_{A_J}} \mathbf{A} \cdot d\mathbf{l} \right] \right\}. \quad (2.3)$$

Owing to the periodicity of the Peierls phase  $\frac{2\pi}{\Phi_0} \int_{\mathbf{R}_{B_I}}^{\mathbf{R}_{A_J}} \mathbf{A} \cdot d\mathbf{l}$ , a hexagonal primitive unit cell becomes an enlarged rectangle along the  $x$ -direction (the armchair direction), as clearly indicated in figure 1.1(a). Furthermore, the hexagonal first Brillouin zone (figure 1.1(b)) is changed into a very small rectangle (figure 1.1(c); an area of  $4\pi^2/3\sqrt{3} b^2 R_B$ ).  $R_B$ , which is related to the period along  $\hat{x}$ , is defined as the ratio of  $\Phi_0$  versus magnetic flux through each hexagon ( $\Phi$ ), e.g.  $R_B = 2 \times 10^3$  at  $B_z = 40$  T. Accordingly, the  $B_z$ -enlarged rectangular cell includes  $4R_B$  atoms ( $2R_B A$  and  $2R_B B$  atoms); its length along the  $x$ -direction is  $l_x = 3R_B b$ . This implies that the Bloch wave functions under a uniform magnetic field can be expressed by the linear superposition of the  $4R_B$  tight-binding functions in the rectangular unit cell:  $|A_{1\mathbf{k}}\rangle$ ,  $|B_{1\mathbf{k}}\rangle$ ,  $|A_{2\mathbf{k}}\rangle$ ,  $|B_{2\mathbf{k}}\rangle$ , ...,  $|A_{2R_B-1\mathbf{k}}\rangle$ ,  $|B_{2R_B-1\mathbf{k}}\rangle$ ,  $|A_{2R_B\mathbf{k}}\rangle$ ;  $|B_{2R_B\mathbf{k}}\rangle$ . Under these bases, the nonzero and independent Hamiltonian matrix elements are given by

$$\langle A_{J,\mathbf{k}}|H|B_{I,\mathbf{k}}\rangle = \gamma_0(t_{1,J} + t_{2,J})\delta_{J,I} + \gamma_0 t_3 \delta_{J,I+1}, \quad (2.4)$$

where the vector-potential-induced phase terms in the hopping integrals are

$$\begin{aligned} t_{1,J} &= \exp \left\{ i \left[ (k_x b/2 + k_y \sqrt{3} b/2) - \pi \frac{\Phi}{\Phi_0} \left( J - 1 + \frac{1}{6} \right) \right] \right\}, \\ t_{2,J} &= \exp \left\{ i \left[ (k_x b/2 - k_y \sqrt{3} b/2) + \pi \frac{\Phi}{\Phi_0} \left( J - 1 + \frac{1}{6} \right) \right] \right\}; \\ t_3 &= \exp(ik_y b). \end{aligned} \quad (2.5)$$

To solve the  $4R_B \times 4R_B$  Hamiltonian matrix more efficiently, a band-like Hamiltonian matrix is introduced by rearranging the bases as the following sequence:  $|A_{1k}\rangle, |B_{2R_B k}\rangle, |B_{1k}\rangle, |A_{2R_B k}\rangle, |A_{2k}\rangle, |B_{2R_B-1k}\rangle, |B_{2k}\rangle, |A_{2R_B-1k}\rangle, \dots$ . As to the  $(k_x = 0, k_y = 0)$  magnetic states, the Hamiltonian matrix elements are real numbers. This numerical characteristic is also revealed in layered graphenes with normal stacking configurations. State energy and wave function,  $E^{c,v}$  and  $\Psi^{c,v}$ , are obtained from diagonalizing the Hamiltonian matrix, where  $c$  and  $v$ , respectively, represent conduction and valence states. In addition, similar equations, as expressed in equations (2.3)–(2.5), can be derived for a modulated/composite magnetic field.

According to the exact diagonalization scheme, the Landau wavefunction can be expressed as

$$|\Psi_k^{c,v}\rangle = \sum_{J=1}^{2R_B} A_J |A_{Jk}\rangle + B_J |B_{Jk}\rangle, \quad (2.6)$$

where the subenvelope function  $A_J(B_J)$  corresponds to the probability amplitude of the tight-binding function based on the  $J$ th  $A(B)$  atom in the enlarged cell. The spatial distribution of subenvelope function will present a special oscillation mode, being very useful in the characterization of each LL. This method has well defined the quantum number of LLs in layered graphenes and other systems discussed in this work. The generalization of the magnetic wave function is valuable in understanding other physical properties, such as the critical mechanisms of quantum transports [2], magneto-optical spectra [3–9] and Coulomb excitations [10–19].

## 2.2 Tetra-layer graphene

ABC-stacked graphene has an interlayer distance of  $d = 3.37 \text{ \AA}$ , as sketched in figure 2.1(a). For an  $N$ -layer system,  $2N$  carbon atoms are included in a primitive unit cell, in which two sublattice atoms in the  $l$ th layer are denoted as  $A^l$  and  $B^l$ . Each graphene sheet is shifted by a distance of  $b$  along the armchair direction with respect to the adjacent layer. The sublattice A(B) of one layer is situated directly above the  $A$  atom of the adjacent lower layer, while the sublattice B(A) lies above the center of its hexagon. The layer-dependent Hamiltonian is characterized by the intralayer and the interlayer atomic interactions  $\beta_i$ 's (figure 2.1(a)), where  $\beta_0$  represents the nearest-neighbor hopping integral within the same layer;  $(\beta_1, \beta_3, \beta_4)$  are between adjacent layers;  $\beta_2$  and  $\beta_5$  are related to the next-neighboring layers.  $\beta_1$  and  $\beta_2$  are couplings between two vertical sites, and  $(\beta_3, \beta_4, \beta_5)$  belong to

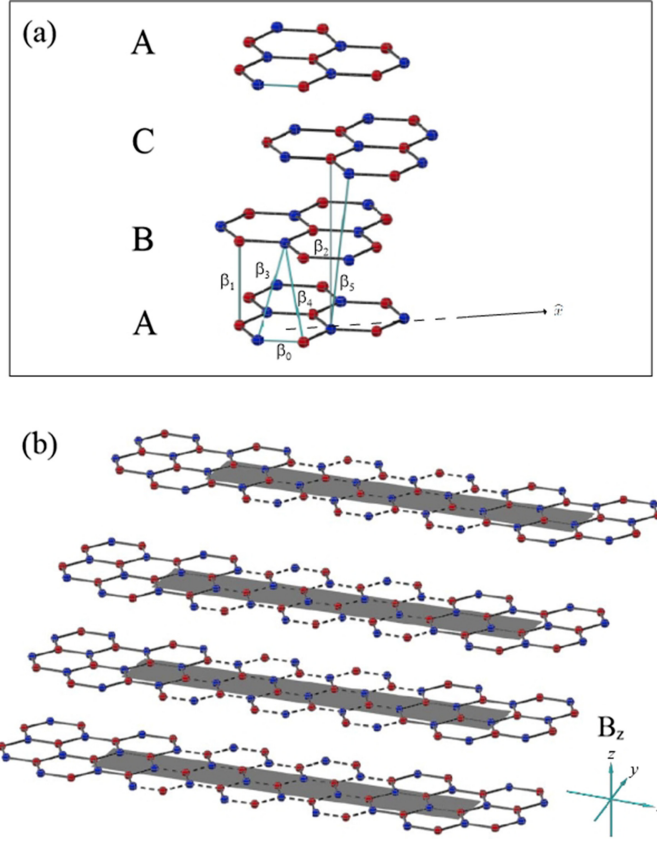


**Figure 2.1.** (a) Geometric structure and (b)  $B_z$ -dependent unit cell of the ABC-stacked tetralayer graphene.  $\beta_i$ 's denote the intralayer and interlayer hopping integrals.

non-vertical interactions. The values of hopping integrals are as follows:  $\beta_0 = -3.16$  eV,  $\beta_1 = 0.36$  eV,  $\beta_2 = -0.01$  eV,  $\beta_3 = 0.32$  eV,  $\beta_4 = 0.03$  eV, and  $\beta_5 = 0.0065$  eV [20].

As to tetra-layer ABC stacking, the zero-field Hamiltonian, being associated with eight carbon atoms in a unit cell, has the block matrix form

$$H_{ABC} = \begin{pmatrix} H_1 & H_2 & H_3 & 0 \\ H_2^* & H_1 & H_2 & H_3 \\ H_3^* & H_2^* & H_1 & H_2 \\ 0 & H_3^* & H_2^* & H_1 \end{pmatrix}, \quad (2.7)$$

where three independent  $2 \times 2$  matrices are

$$H_1 = \begin{pmatrix} 0 & \beta_0 f(k_x, k_y) \\ \beta_0 f^*(k_x, k_y) & 0 \end{pmatrix}, \quad (2.8)$$

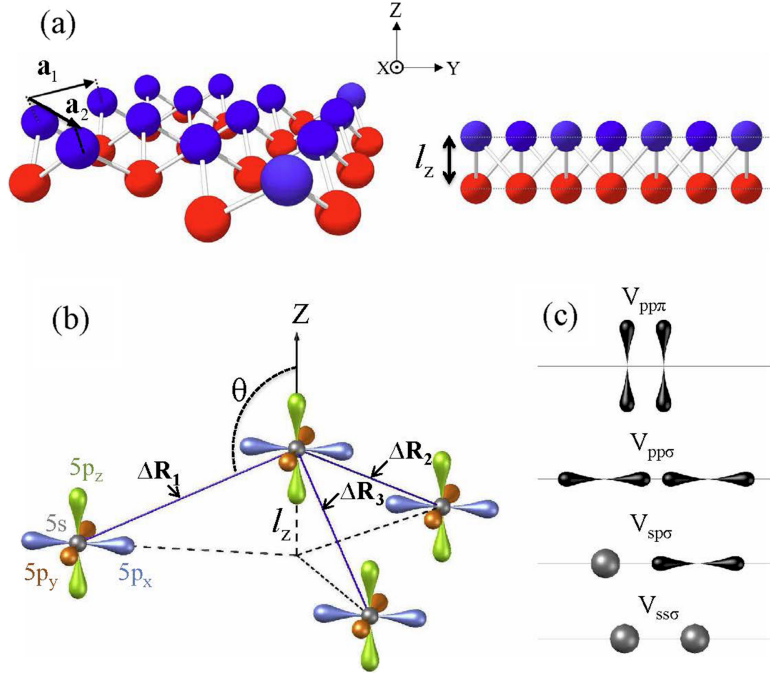


**Figure 2.2.** (a) Geometric structure of the buckled (silicene, germanene, tinene) with (b) the  $sp^3$  bondings, or (c) significant orbital hybridizations.

$$H_2 = \begin{pmatrix} \beta_4 f^*(k_x, k_y) & \beta_1 \\ \beta_3 f(k_x, k_y) & \beta_4 f^*(k_x, k_y) \end{pmatrix}; \quad (2.9)$$

$$H_3 = \begin{pmatrix} \beta_5 f(k_x, k_y) & \beta_5 f^*(k_x, k_y) \\ \beta_2 & \beta_5 f(k_x, k_y) \end{pmatrix}. \quad (2.10)$$

The summation of the nearest-neighbor phase terms is  $f(k_x, k_y) = \sum_{j=1}^3 \exp(i\mathbf{k} \cdot \mathbf{r}_j) = \exp(ik_x) + \exp(ik_x/2)\cos(\sqrt{3}bk_y/2)$ . The diagonal matrix elements are changed from zero into finite values in the presence of a uniform perpendicular electric field; that is,  $E_z$  leads to the Coulomb potential energy differences in distinct layers. For experimental measurements, this field can be created by the application of gate voltage ( $V_z$ ) across the layered systems.

The periodical Peierls phase in tetra-layer ABC stacking can create an enlarged rectangle with  $16R_B$  atoms. The magnetic Hamiltonian is constructed from the  $16R_B$  tight-binding functions  $\{|A_{1\mathbf{k}}^1\rangle, |B_{1\mathbf{k}}^1\rangle, |A_{1\mathbf{k}}^2\rangle, |B_{1\mathbf{k}}^2\rangle \dots |A_{1\mathbf{k}}^4\rangle, |B_{1\mathbf{k}}^4\rangle \dots |A_{2R_B\mathbf{k}}^4\rangle, |B_{2R_B\mathbf{k}}^4\rangle\}$  based on the periodical atoms in the rectangular unit cell (figure 2.1(b)). By the detailed calculations, the non-vanishing Hamiltonian matrix elements associated with the hopping integrals  $\beta_i$ 's cover

$$\langle B_{jk}^1 | H | A_{lk}^1 \rangle = \langle B_{jk}^4 | H | A_{lk}^4 \rangle = \beta_0(t_{1,I}\delta_{I,J} + q\delta_{I,J+1}), \quad (2.11)$$

$$\langle B_{jk}^2 | H | A_{lk}^2 \rangle = \beta_0(t_{3,I}\delta_{I,J-1} + q\delta_{I,J}), \quad (2.12)$$

$$\langle B_{jk}^3 | H | A_{lk}^3 \rangle = \beta_0(t_{2,I}\delta_{I,J} + q\delta_{I,J+1}), \quad (2.13)$$

$$\langle A_{jk}^1 | H | B_{lk}^2 \rangle = \langle A_{jk}^2 | H | B_{lk}^3 \rangle = \langle A_{jk}^3 | H | B_{lk}^4 \rangle = \beta_1\delta_{I,J}, \quad (2.14)$$

$$\langle B_{jk}^1 | H | A_{lk}^3 \rangle = \langle B_{jk}^2 | H | A_{lk}^4 \rangle = \beta_2\delta_{I,J}, \quad (2.15)$$

$$\langle A_{jk}^2 | H | B_{lk}^1 \rangle = \beta_3(t_{2,I}\delta_{I,J} + q\delta_{I,J+1}), \quad (2.16)$$

$$\langle A_{jk}^4 | H | B_{lk}^3 \rangle = \beta_3(t_{3,I}\delta_{I,J-1} + q\delta_{I,J}), \quad (2.17)$$

$$\langle A_{jk}^3 | H | B_{lk}^2 \rangle = \beta_3(t_{1,I}\delta_{I,J} + q\delta_{I,J+1}), \quad (2.18)$$

$$\langle B_{jk}^1 | H | B_{lk}^2 \rangle = \langle A_{jk}^3 | H | A_{lk}^4 \rangle = \beta_4(t_{1,I}\delta_{I,J} + q\delta_{I,J+1}), \quad (2.19)$$

$$\langle A_{jk}^1 | H | A_{lk}^2 \rangle = \langle B_{jk}^2 | H | B_{lk}^3 \rangle = \beta_4(t_{3,I}\delta_{I,J-1} + q\delta_{I,J}), \quad (2.20)$$

$$\langle A_{jk}^2 | H | A_{lk}^3 \rangle = \langle B_{jk}^3 | H | B_{lk}^4 \rangle = \beta_4(t_{2,I}\delta_{I,J} + q\delta_{I,J+1}), \quad (2.21)$$

$$\langle B_{jk}^3 | H | B_{lk}^1 \rangle = \langle A_{jk}^2 | H | B_{lk}^4 \rangle = \beta_5(t_{2,I}\delta_{I,J} + q\delta_{I,J+1}), \quad (2.22)$$

$$\langle A_{jk}^3 | H | A_{lk}^1 \rangle = \langle B_{jk}^4 | H | B_{lk}^2 \rangle = \beta_5(t_{1,I}\delta_{I,J} + q\delta_{I,J+1}), \quad (2.23)$$

$$\langle A_{jk}^1 | H | B_{lk}^3 \rangle = \langle A_{jk}^4 | H | A_{lk}^2 \rangle = \beta_5(t_{3,I}\delta_{I,J-1} + q\delta_{I,J}). \quad (2.24)$$

The four independent phase terms are

$$\begin{aligned} t_{1,I} &= \exp \left\{ i \left[ -(k_x b/2) - (\sqrt{3} k_y b/2) + \pi \Phi(I - 1 + 1/6) \right] \right\} \\ &\quad + \exp \left\{ i \left[ -(k_x b/2) + (\sqrt{3} k_y b/2) - \pi \Phi(I - 1 + 1/6) \right] \right\}, \\ t_{2,I} &= \exp \left\{ i \left[ -(k_x b/2) - (\sqrt{3} k_y b/2) + \pi \Phi(I - 1 + 3/6) \right] \right\} \\ &\quad + \exp \left\{ i \left[ -(k_x b/2) + (\sqrt{3} k_y b/2) - \pi \Phi(I - 1 + 3/6) \right] \right\}, \\ t_{3,I} &= \exp \left\{ i \left[ -(k_x b/2) - (\sqrt{3} k_y b/2) + \pi \Phi(I - 1 + 5/6) \right] \right\} \\ &\quad + \exp \left\{ i \left[ -(k_x b/2) + (\sqrt{3} k_y b/2) - \pi \Phi(I - 1 + 5/6) \right] \right\}, \\ \text{and } q &= \exp \{ i k_x b \}. \end{aligned}$$

In order to enhance the computation efficiency, we choose the bases of  $\{|A_{1k}^1\rangle, |B_{1k}^2\rangle, |A_{1k}^3\rangle, |B_{1k}^4\rangle, |B_{1k}^1\rangle, |A_{1k}^2\rangle, |B_{1k}^3\rangle, |A_{1k}^4\rangle, \dots, |B_{2R_Bk}^1\rangle, |A_{2R_Bk}^2\rangle, |B_{2R_Bk}^3\rangle, |A_{2R_Bk}^4\rangle\}$  to arrange the Hamiltonian as a band-like symmetric matrix. This allows an efficient numerical solution of the eigenvalues and eigenfunctions, even for a small magnetic field strength and a huge  $R_B$ . The analytic formulas for the Hamiltonian matrix elements could also be obtained for any  $N$ -layer systems with the normal stacking configurations (AAA, ABA, ABC and AAB). Furthermore, such matrix elements remain similar under a composite  $B_z$ - and  $E_z$ -field.

### 2.3 Tinene

The generalized tight-binding model is further developed to include  $sp^3$  orbital bonding, SOC, and the external fields simultaneously. Monolayer buckled tinene, as shown in figure 2.2(a), consists of two equivalent A and B sublattices, respectively, situated at two parallel planes with a separation of  $l_z = 0.417 \text{ \AA}$ . The primitive unit vectors are  $\mathbf{a}_1$  and  $\mathbf{a}_2$  with a lattice constant of  $a = 4.7 \text{ \AA}$ , and the angle between the Sn-Sn bond and the  $z$ -axis is  $\theta = 107.1^\circ$  (figure 2.2(b)). The  $5s$  orbital energy is  $E_{5s} = -6.23 \text{ eV}$  below that of the  $5p$  orbitals taken as zero ( $E_{5p} = 0$ ). The Slater–Koster hopping parameters in the  $sp^3$  bonding are  $V_{ss\sigma} = -2.62 \text{ eV}$ ,  $V_{sp\sigma} = 2.65 \text{ eV}$ ,  $V_{pp\sigma} = 1.49 \text{ eV}$ , and  $V_{pp\pi} = -0.79 \text{ eV}$ . Such significant chemical bondings are clearly indicated in figure 2.2(c). The SOC strength ( $\lambda_{\text{SOC}} = 0.8 \text{ eV}$ ) of tinene is predicted to be two orders of magnitude greater than that of graphene [21, 22]. In the orbital- and spin-dependent bases of  $\{|5p_z^A\rangle, |5p_x^A\rangle, |5p_y^A\rangle, |5s^A\rangle, |5p_z^B\rangle, |5p_x^B\rangle, |5p_y^B\rangle, |5s^B\rangle\} \otimes \{\uparrow, \downarrow\}$ , the Hamiltonian, with the nearest-neighbor atomic interactions, presents two types of site-dominated matrix elements:

$$\begin{aligned} \langle A_{om}|H|B_{o'm'}\rangle &= \sum_{\Delta\mathbf{R}_J} \gamma_{oo'}^{\Delta\mathbf{R}_J} \exp i\mathbf{k} \cdot \Delta\mathbf{R}_J \delta_{mm'}, \\ \langle A_{om}|H|A_{om}\rangle &= \langle B_{om}|H|B_{om}\rangle = E_o, \end{aligned} \quad (2.25)$$

where  $o(o')$ ,  $m(m')$ ,  $\Delta\mathbf{R}_J$  and  $E_o$  stand for the atomic orbital, spin, the translation vector of the nearest-neighbor atom, and site energy, respectively. The nearest-neighbor hopping integral ( $\gamma_{oo'}^{\Delta\mathbf{R}_J}$ ) depends on the type of atomic orbitals,  $\Delta\mathbf{R}_J$ , and  $\theta$ .  $\gamma_{oo'}^{\Delta\mathbf{R}_J}$ s for the three nearest-neighbor atoms and different atomic orbitals are given by



$$\begin{aligned}
 \gamma_{xx}^{\Delta\mathbf{R}_1} &= V_{pp\sigma} + (V_{pp\pi} - V_{pp\sigma})\cos^2\theta, \\
 \gamma_{xx}^{\Delta\mathbf{R}_2} &= \gamma_{xx}^{\Delta\mathbf{R}_3} = V_{pp\pi} + \frac{1}{4}(V_{pp\pi} - V_{pp\sigma})\sin^2\theta, \\
 \gamma_{xy}^{\Delta\mathbf{R}_1} &= 0, \\
 \gamma_{xy}^{\Delta\mathbf{R}_2} &= -\gamma_{xy}^{\Delta\mathbf{R}_3} = \frac{\sqrt{3}}{4}(V_{pp\pi} - V_{pp\sigma})\sin^2\theta, \\
 \gamma_{xz}^{\Delta\mathbf{R}_1} &= (V_{pp\pi} - V_{pp\sigma})\sin\theta\cos\theta, \\
 \gamma_{xz}^{\Delta\mathbf{R}_2} &= \gamma_{xz}^{\Delta\mathbf{R}_3} = -\frac{1}{2}(V_{pp\pi} - V_{pp\sigma})\sin\theta\cos\theta, \\
 \gamma_{xs}^{\Delta\mathbf{R}_1} &= V_{sp\sigma}\sin\theta, \\
 \gamma_{xs}^{\Delta\mathbf{R}_2} &= \gamma_{xs}^{\Delta\mathbf{R}_3} = -\frac{1}{2}V_{sp\sigma}\sin\theta, \\
 \gamma_{yy}^{\Delta\mathbf{R}_1} &= V_{pp\pi}, \\
 \gamma_{yy}^{\Delta\mathbf{R}_2} &= \gamma_{yy}^{\Delta\mathbf{R}_3} = V_{pp\pi} + \frac{3}{4}(V_{pp\pi} - V_{pp\sigma})\sin^2\theta, \\
 \gamma_{yz}^{\Delta\mathbf{R}_1} &= 0, \\
 \gamma_{yz}^{\Delta\mathbf{R}_2} &= -\gamma_{yz}^{\Delta\mathbf{R}_3} = \frac{\sqrt{3}}{2}(V_{pp\sigma} - V_{pp\pi})\sin\theta\cos\theta, \\
 \gamma_{ys}^{\Delta\mathbf{R}_1} &= 0, \\
 \gamma_{ys}^{\Delta\mathbf{R}_2} &= -\gamma_{ys}^{\Delta\mathbf{R}_3} = -\frac{\sqrt{3}}{2}V_{sp\sigma}\sin\theta, \\
 \gamma_{zz}^{\Delta\mathbf{R}_1} &= \gamma_{zz}^{\Delta\mathbf{R}_2} = \gamma_{zz}^{\Delta\mathbf{R}_3} = V_{pp\pi} + (V_{pp\sigma} - V_{pp\pi})\cos^2\theta, \\
 \gamma_{zs}^{\Delta\mathbf{R}_1} &= \gamma_{zs}^{\Delta\mathbf{R}_2} = \gamma_{zs}^{\Delta\mathbf{R}_3} = -V_{sp\sigma}\cos\theta; \\
 \gamma_{ss}^{\Delta\mathbf{R}_1} &= \gamma_{ss}^{\Delta\mathbf{R}_2} = \gamma_{ss}^{\Delta\mathbf{R}_3} = V_{ss\sigma}.
 \end{aligned} \tag{2.26}$$

It should be noted that the strong  $sp^3$  hybridization not only causes the hoppings between  $5p_z$  and  $(5p_x, 5p_y, 5s)$  orbitals, e.g.  $\gamma_{zx}^{\Delta\mathbf{R}_1} = (V_{pp\pi} - V_{pp\sigma})\sin\theta\cos\theta$ , but also results in the non-parallel misorientation of  $p\pi$  orbitals ( $\gamma_{zz}^{\Delta\mathbf{R}_j} = V_{pp\pi}\sin^2\theta + V_{pp\sigma}\cos^2\theta$ ). The SOC interaction under the Coulomb central potential,  $V_{\text{SOC}} = \lambda_{\text{SOC}}\mathbf{L} \cdot \mathbf{S}$ , can also be expressed as

$$V_{\text{SOC}} = \lambda_{\text{SOC}} \left( \frac{L_+s_- + L_-s_+}{2} + L_zs_z \right), \tag{2.27}$$

where  $L_{\pm} = L_x \pm iL_y$  ( $s_{\pm} = s_x \pm is_y$ ) is the ladder operator for the angular momentum (spin). Such operators will play an important role in the spin-dependent Hamiltonian. The  $5p_z$  orbital and the composite orbitals of  $\frac{1}{\sqrt{2}}(5p_x \pm i5p_y)$  correspond to the magnetic quantum number of 0 and  $\pm 1$ , respectively. Therefore, the SOC between the

$5p_z$  and  $(5p_x, 5p_y)$  orbitals leads to the splitting of states and an interchange of spin configurations, whereas that between the  $5p_x$  and  $5p_y$  orbitals causes the splitting of states with opposite spin configurations. In the calculations, only the intra-atomic  $V_{\text{SOC}}$  is considered and the related matrix elements are

$$\langle A_{p_\alpha, m} | V_{\text{SOC}} | A_{p_\beta, m'} \rangle = \langle B_{p_\alpha, m} | V_{\text{SOC}} | B_{p_\beta, m'} \rangle = \frac{\lambda_{\text{SOC}}}{2} (-i\varepsilon_{\alpha\beta\gamma} \sigma_{mm'}^\gamma), \quad (2.28)$$

where  $(\alpha, \beta, \gamma)$  denote the  $(x, y, z)$  directions,  $\varepsilon$  is the permutation operator, and  $\sigma$  the Pauli spin matrix.

In the Landau gauge  $\mathbf{A} = (0, B_z x, 0)$ , an enlarged rectangle includes  $4R_B$  ( $4 \times 21665/B_z$ ;  $B_z$  in unit of T) Sn atoms; furthermore, four orbitals and two spin configurations need to be taken into consideration. As a result, the magnetic Hamiltonian is the linear superposition of the  $32R_B$  tight-binding functions  $\{|A_{Jom}\rangle; |B_{Jom}\rangle | J = 1, 2, \dots, 2R_B; o = 5p_x, 5p_y, 5p_z, 5s; m = \uparrow, \downarrow\}$ . The independent Hamiltonian matrix elements are characterized by

$$\langle A_{Jom} | H | B_{I'o'm} \rangle = (\gamma_{oo'}^{\Delta \mathbf{R}_1} t_1 + \gamma_{oo'}^{\Delta \mathbf{R}_2} t_2) \delta_{J,I} + \gamma_{oo'}^{\Delta \mathbf{R}_3} t_3 \delta_{J,I+1}, \quad (2.29)$$

where the three position-dependent phases,  $t_1$ ,  $t_2$ , and  $t_3$ , are similar to those of monolayer graphene (equation (2.5)). Most of the matrix elements are complex numbers even for the  $(k_x = 0, k_y = 0)$  LL state, in contrast with those of layered graphenes. Numerical calculations will become more difficult in multi-orbital bonding systems. A perpendicular electric field in buckled monolayer tinene will dramatically change electronic properties. Moreover, similar calculations, being sensitive to the strength of orbital hybridization and SOC, could also be made for silicene and germanene.

## 2.4 Monolayer and bilayer phosphorenes

Monolayer phosphorene, with a puckered honeycomb structure, has a primitive unit cell containing four phosphorus atoms, as indicated by the dashed green lines in figure 2.3(a). Two of the four phosphorus atoms are located on the lower (magenta circles) or upper (blue circles) sublattice sites. The two bond lengths for in-plane and inter-plane P-P connections are  $b_1 = 2.24 \text{ \AA}$  and  $b_2 = 2.22 \text{ \AA}$ , respectively. The angle between two in-plane bonds is  $\alpha' = 100.7^\circ$ , and that between the inter-plane bond and the  $x$ -axis is  $\beta' = 69.2^\circ$ . The lattice vectors are  $\mathbf{a}_1 = 2b_1 \sin(\frac{\alpha'}{2}) \hat{y}$  and  $\mathbf{a}_2 = [b_2 \cos(\beta') + 2b_1 \cos(\frac{\alpha'}{2})] \hat{x}$ , as indicated by the green arrows in figure 2.3(a). For bilayer phosphorene, AB stacking is the most stable configuration, as revealed in black phosphorus. Such stacking could be regarded as shifting the bottom layer by half of the cell along either  $\mathbf{a}_1$  or  $\mathbf{a}_2$  direction. As a result, the edge corresponds to the center for the puckered hexagons in two neighboring layers, or vice versa.

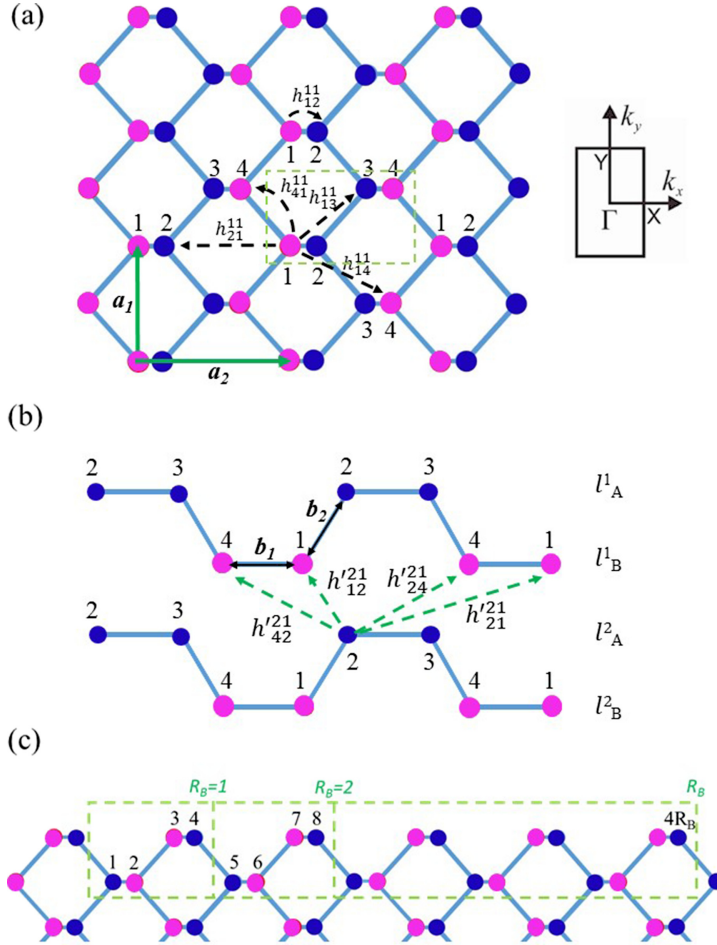


**Figure 2.3.** Geometric structures of (a) monolayer and (b) bilayer phosphorenes, respectively, for the top and side views with the intralayer and interlayer hopping integrals. (c) The magnetically enlarged unit cell of monolayer system.

The low-lying electronic structure is mainly from the  $3p_z$ -orbital hybridizations. The Hamiltonian of monolayer phosphorene (bilayer AB stacking) is a  $4 \times 4$  ( $8 \times 8$ ) Hermitian matrix. The significant atomic interactions include the position-dependent five intralayer  $h_{IJ}^{ll}$  and four interlayer  $h_{IJ}^{ll'} (l \neq l')$  hopping integrals. The former, as clearly shown by the dashed black arrows in figure 2.3(a), are  $h_{12}^{11} = 3.665$  eV,  $h_{21}^{11} = -0.055$  eV,  $h_{13}^{11} = -0.105$  eV,  $h_{14}^{11} = -0.205$  eV, and  $h_{41}^{11} = -1.22$  eV. The latter (figure 2.3(b)) are  $h_{12}^{21} = 0.295$  eV,  $h_{21}^{21} = -0.091$  eV,  $h_{24}^{21} = -0.151$  eV, and  $h_{42}^{21} = 0.273$  eV. The matrix elements related to the intra-layer interactions are given by:

$$\begin{aligned}
 \langle B_{I\mathbf{k}}^I | H | A_{J\mathbf{k}}^{I'} \rangle &= \langle A_{I\mathbf{k}}^I | H | B_{J\mathbf{k}}^{I'} \rangle = (h_{12}^{11} t_2' + h_{21}^{11} t_5') \delta_{I+1, J} \delta_{I, I'}, \\
 \langle B_{I\mathbf{k}}^I | H | A_{J\mathbf{k}}^{I'} \rangle &= \langle A_{I\mathbf{k}}^I | H | B_{J\mathbf{k}}^{I'} \rangle = (h_{13}^{11} t_4' + h_{13}^{11} t t_4') \delta_{I+2, J} \delta_{I, I'}, \\
 \langle B_{I\mathbf{k}}^I | H | B_{J\mathbf{k}}^{I'} \rangle &= (h_{41}^{11} t t_1' + h_{14}^{11} t_3') \delta_{I+3, J} \delta_{I, I'}, \\
 \langle B_{I\mathbf{k}}^I | H | B_{J\mathbf{k}}^{I'} \rangle &= (h_{41}^{11} t_1' + h_{14}^{11} t_3') \delta_{I, J+3} \delta_{I, I'}, \\
 \langle A_{I\mathbf{k}}^I | H | A_{J\mathbf{k}}^{I'} \rangle &= (h_{41}^{11} t t_1' + h_{14}^{11} t_3') \delta_{I, J-1} \delta_{I, I'}, \\
 \langle A_{I\mathbf{k}}^I | H | A_{J\mathbf{k}}^{I'} \rangle &= (h_{41}^{11} t t_1' + h_{14}^{11} t t_3') \delta_{I+1, J} \delta_{I, I'},
 \end{aligned} \tag{2.30}$$

where  $I = 1, 2, 3, 4$ . The position-dependent phase terms for the intralayer hoppings are written below:

$$\begin{aligned}
 t_1' &= \exp i(k_x d_{1x} + k_y d_{1y}) + \exp i(k_x d_{1x} - k_y d_{1y}), \\
 t t_1' &= \exp i(-k_x d_{1x} + k_y d_{1y}) + \exp i(-k_x d_{1x} - k_y d_{1y}), \\
 t_2' &= \exp i(k_x d_{2x}), \\
 t_3' &= \exp i(k_x d_{3x} + k_y d_{1y}) + \exp i(k_x d_{3x} - k_y d_{1y}), \\
 t t_3' &= \exp i(-k_x d_{3x} + k_y d_{1y}) + \exp i(-k_x d_{3x} - k_y d_{1y}), \\
 t_4' &= \exp i(k_x d_{4x} + k_y d_{1y}) + \exp i(k_x d_{4x} - k_y d_{1y}), \\
 t t_4' &= \exp i(-k_x d_{4x} + k_y d_{1y}) + \exp i(-k_x d_{4x} - k_y d_{1y}), \\
 t_5' &= \exp i(-k_x d_{5x}),
 \end{aligned} \tag{2.31}$$

where  $d_{1x-5x}$  ( $d_{1y}$ ) is the corresponding distance along the  $x$  ( $y$ )-axis between the interacting lattice sites. These distance parameters are expressed below:

$$\begin{aligned}
 d_{1x} &= b_1 \cos\left(\frac{\alpha'}{2}\right), \\
 d_{2x} &= b_2 \cos\beta', \\
 d_{3x} &= b_1 \cos\left(\frac{\alpha'}{2}\right) + 2b_2 \cos\beta', \\
 d_{4x} &= b_1 \cos\left(\frac{\alpha'}{2}\right) + b_2 \cos\beta', \\
 d_{5x} &= 2b_1 \cos\left(\frac{\alpha'}{2}\right) + b_2 \cos\beta'; \\
 d_{1y} &= b_1 \sin\left(\frac{\alpha'}{2}\right).
 \end{aligned} \tag{2.32}$$

As for interlayer interactions, the independent Hamiltonian matrix elements are:

$$\begin{aligned}
 \langle A_{I\mathbf{k}}^I | H | B_{J\mathbf{k}}^{I'} \rangle &= (h_{42}^{21} t t_2'' + h_{42}^{21} t_2'' + h_{24}^{21} t t_3'' + h_{24}^{21} t_3'') \delta_{I+1, J} \delta_{I, I'+1}, \\
 \langle A_{I\mathbf{k}}^I | H | B_{J\mathbf{k}}^{I'} \rangle &= (h_{42}^{21} t t_2'' + h_{42}^{21} t_2'' + h_{24}^{21} t t_3'' + h_{24}^{21} t_3'') \delta_{I, J+2} \delta_{I, I'+1}, \\
 \langle A_{I\mathbf{k}}^I | H | B_{J\mathbf{k}}^{I'} \rangle &= (h_{12}^{21} t t_1'' + h_{21}^{21} t_4'') \delta_{I, J+1} \delta_{I, I'+1}; \\
 \langle A_{I\mathbf{k}}^I | H | B_{J\mathbf{k}}^{I'} \rangle &= (h_{12}^{21} t_1'' + h_{21}^{21} t t_4'') \delta_{I+1, J} \delta_{I, I'+1}.
 \end{aligned} \tag{2.33}$$

The position-dependent phase terms for the interlayer hoppings are as follows:

$$\begin{aligned}
 t_1'' &= \exp i(k_x d_{2x} + k_y d_{1y}) + \exp i(k_x d_{2x} - k_y d_{1y}), \\
 tt_1'' &= \exp i(-k_x d_{2x} + k_y d_{1y}) + \exp i(-k_x d_{2x} - k_y d_{1y}), \\
 t_2'' &= \exp i(k_x d_{4x}), \\
 tt_2'' &= \exp i(-k_x d_{4x}), \\
 t_3'' &= \exp i(k_x d_{4x} + k_y 2d_{1y}) + \exp i(k_x d_{4x} - k_y 2d_{1y}), \\
 tt_3'' &= \exp i(-k_x d_{4x} + k_y 2d_{1y}) + \exp i(-k_x d_{4x} - k_y 2d_{1y}), \\
 t_4'' &= \exp i(k_x d_{5x} + k_y d_{1y}) + \exp i(k_x d_{5x} - k_y d_{1y}); \\
 tt_4'' &= \exp i(-k_x d_{5x} + k_y d_{1y}) + \exp i(-k_x d_{5x} - k_y d_{1y}).
 \end{aligned} \tag{2.34}$$

When monolayer and bilayer phosphorene systems exist in a perpendicular magnetic field, the magnetic flux through a puckered hexagon is  $\Phi = a_1 a_2 B_z / 2$ . The vector potential,  $\mathbf{A} = (B_z x) \hat{y}$ , leads to a new period along  $\hat{x}$  and thus an enlarged rectangular unit cell with  $4R_B = 4\Phi_0 / \Phi$  atoms in monolayer, as illustrated in figure 2.3(c). The reduced first Brillouin zone has an area of  $4\pi^2 a_1 a_2 R_B$ . For bilayer phosphorene, the magnetic Hamiltonian matrix is very large with  $8R_B \times 8R_B$  matrix elements within achievable experimental field strengths, e.g. the dimension of 16 800 at  $B_z = 30$  T. The magnetic matrix elements can be obtained by replacing the phase terms in equation (2.31) by those with extra Peierls phases, as given below:

(I) intralayer interactions:

$$\begin{aligned}
 tt'_{1,I=\text{odd}} &= \exp i \left( -k_x d_{1x} + k_y d_{1y} + \pi \frac{\Phi}{\Phi_0} \left( I - 1 + \frac{2d_{2x} - d_{3x}}{d_{4x}} \right) \right) \\
 &\quad + \exp i \left( k_x d_{1x} - k_y d_{1y} - \pi \frac{\Phi}{\Phi_0} \left( I - 1 + \frac{2d_{2x} - d_{3x}}{2d_{4x}} \right) \right), \\
 t'_{3,I=\text{odd}} &= \exp i \left( k_x d_{3x} + k_y d_{1y} + \pi \frac{\Phi}{\Phi_0} \left( I - 1 + \frac{2d_{2x} + d_{1x}}{2d_{4x}} \right) \right) \\
 &\quad + \exp i \left( k_x d_{3x} - k_y d_{1y} + \pi \frac{\Phi}{\Phi_0} \left( I - 1 + \frac{2d_{2x} + d_{1x}}{2d_{4x}} \right) \right), \\
 tt'_{3,I=\text{odd}} &= \exp i \left( -k_x d_{3x} + k_y d_{1y} + \pi \frac{\Phi}{\Phi_0} \left( I - 1 - \frac{2d_{2x} + d_{1x}}{2d_{4x}} \right) \right) \\
 &\quad + \exp i \left( -k_x d_{3x} - k_y d_{1y} - \pi \frac{\Phi}{\Phi_0} \left( I - 1 - \frac{2d_{2x} + d_{1x}}{2d_{4x}} \right) \right), \\
 t'_{4,I=\text{odd}} &= \exp i \left( k_x d_{4x} + k_y d_{1y} + \pi \frac{\Phi}{\Phi_0} \left( I - \frac{1}{2} \right) \right) \\
 &\quad + \exp i \left( k_x d_{4x} - k_y d_{1y} - \pi \frac{\Phi}{\Phi_0} \left( I - \frac{1}{2} \right) \right),
 \end{aligned} \tag{2.35}$$

$$\begin{aligned}
 tt'_{4,I=\text{odd}} &= \exp i \left( -k_x d_{4x} + k_y d_{1y} + \pi \frac{\Phi}{\Phi_0} \left( I - \frac{3}{2} \right) \right) \\
 &\quad + \exp i \left( -k_x d_{4x} - k_y d_{1y} - \pi \frac{\Phi}{\Phi_0} \left( I - \frac{3}{2} \right) \right), \\
 t'_{4,I=\text{even}} &= \exp i \left( k_x d_{4x} + k_y d_{1y} + \pi \frac{\Phi}{\Phi_0} \left( I - 1 + \frac{2d_{2x} + d_{4x}}{2d_{4x}} \right) \right) \\
 &\quad + \exp i \left( k_x d_{4x} - k_y d_{1y} - \pi \frac{\Phi}{\Phi_0} \left( I - 1 + \frac{2d_{2x} + d_{4x}}{2d_{4x}} \right) \right), \\
 tt'_{4,I=\text{even}} &= \exp i \left( -k_x d_{4x} + k_y d_{1y} + \pi \frac{\Phi}{\Phi_0} \left( I - 1 - \frac{2d_{2x} + d_{4x}}{2d_{4x}} \right) \right) \\
 &\quad + \exp i \left( -k_x d_{4x} - k_y d_{1y} - \pi \frac{\Phi}{\Phi_0} \left( I - 1 - \frac{2d_{2x} + d_{4x}}{2d_{4x}} \right) \right), \\
 t'_{1,I=\text{even}} &= \exp i \left( k_x d_{1x} + k_y d_{1y} + \pi \frac{\Phi}{\Phi_0} \left( I - 1 + \frac{2d_{2x} + d_{1x}}{2d_{4x}} \right) \right) \\
 &\quad + \exp i \left( k_x d_{1x} - k_y d_{1y} - \pi \frac{\Phi}{\Phi_0} \left( I - 1 + \frac{2d_{2x} + d_{1x}}{2d_{4x}} \right) \right); \\
 tt'_{3,I=\text{even}} &= \exp i \left( -k_x d_{3x} + k_y d_{1y} + \pi \frac{\Phi}{\Phi_0} \left( I - 1 + \frac{2d_{2x} - d_{3x}}{2d_{4x}} \right) \right) \\
 &\quad + \exp i \left( -k_x d_{3x} - k_y d_{3y} - \pi \frac{\Phi}{\Phi_0} \left( I - 1 + \frac{2d_{2x} - d_{3x}}{2d_{4x}} \right) \right).
 \end{aligned} \tag{2.36}$$

(II) interlayer interactions:

$$\begin{aligned}
 t''_{1,I=\text{odd}} &= \exp i \left( k_x d_{2x} + k_y d_{1y} + \pi \frac{\Phi}{\Phi_0} \left( I - 1 + \frac{d_{2x}}{2d_{4x}} \right) \right) \\
 &\quad + \exp i \left( k_x d_{2x} - k_y d_{1y} - \pi \frac{\Phi}{\Phi_0} \left( I - 1 + \frac{d_{2x}}{2d_{4x}} \right) \right), \\
 tt''_{1,I=\text{odd}} &= \exp i \left( -k_x d_{2x} + k_y d_{1y} + \pi \frac{\Phi}{\Phi_0} \left( I - 1 - \frac{d_{2x}}{2d_{4x}} \right) \right) \\
 &\quad + \exp i \left( -k_x d_{2x} - k_y d_{1y} - \pi \frac{\Phi}{\Phi_0} \left( I - 1 - \frac{d_{2x}}{2d_{4x}} \right) \right), \\
 t''_{1,I=\text{even}} &= \exp i \left( k_x d_{2x} + k_y d_{1y} + \pi \frac{\Phi}{\Phi_0} \left( I - 1 - \frac{d_{2x}}{2d_{4x}} \right) \right) \\
 &\quad + \exp i \left( k_x d_{2x} - k_y d_{1y} - \pi \frac{\Phi}{\Phi_0} \left( I - 1 - \frac{d_{2x}}{2d_{4x}} \right) \right),
 \end{aligned}$$

$$\begin{aligned}
 tt''_{1,I=\text{even}} &= \exp i \left( -k_x d_{2x} + k_y d_{1y} + \pi \frac{\Phi}{\Phi_0} \left( I - 1 + \frac{d_{2x}}{2d_{4x}} \right) \right) \\
 &\quad + \exp i \left( -k_x d_{2x} - k_y d_{1y} - \pi \frac{\Phi}{\Phi_0} \left( I - 1 + \frac{d_{2x}}{2d_{4x}} \right) \right), \\
 t''_{3,I=\text{odd}} &= \exp i \left( k_x d_{4x} + k_y 2d_{1y} + 2\pi \frac{\Phi}{\Phi_0} \left( I - \frac{1}{2} \right) \right) \\
 &\quad + \exp i \left( k_x d_{4x} - k_y 2d_{1y} - 2\pi \frac{\Phi}{\Phi_0} \left( I - \frac{1}{2} \right) \right), \\
 tt''_{3,I=\text{odd}} &= \exp i \left( -k_x d_{4x} + k_y 2d_{1y} + 2\pi \frac{\Phi}{\Phi_0} \left( I - \frac{3}{2} \right) \right) \\
 &\quad + \exp i \left( -k_x d_{4x} - k_y 2d_{1y} - 2\pi \frac{\Phi}{\Phi_0} \left( I - \frac{3}{2} \right) \right), \\
 t''_{3,I=\text{even}} &= \exp i \left( k_x d_{4x} + k_y 2d_{1y} + 2\pi \frac{\Phi}{\Phi_0} \left( I - 1 + \frac{2d_{2x} + d_{4x}}{2d_{4x}} \right) \right) \\
 &\quad + \exp i \left( k_x d_{4x} - k_y 2d_{1y} - 2\pi \frac{\Phi}{\Phi_0} \left( I - 1 + \frac{2d_{2x} + d_{4x}}{2d_{4x}} \right) \right), \\
 tt''_{3,I=\text{even}} &= \exp i \left( -k_x d_{4x} + k_y 2d_{1y} + 2\pi \frac{\Phi}{\Phi_0} \left( I - 1 - \frac{2d_{2x} + d_{4x}}{2d_{4x}} \right) \right) \\
 &\quad + \exp i \left( -k_x d_{4x} - k_y 2d_{1y} - 2\pi \frac{\Phi}{\Phi_0} \left( I - 1 - \frac{2d_{2x} + d_{4x}}{2d_{4x}} \right) \right), \\
 t''_{4,I=\text{odd}} &= \exp i \left( k_x d_{5x} + k_y d_{1y} + \pi \frac{\Phi}{\Phi_0} \left( I - 1 - \frac{d_{5x}}{2d_{4x}} \right) \right) \\
 &\quad + \exp i \left( k_x d_{5x} - k_y d_{1y} - \pi \frac{\Phi}{\Phi_0} \left( I - 1 - \frac{d_{5x}}{2d_{4x}} \right) \right), \\
 tt''_{4,I=\text{odd}} &= \exp i \left( -k_x d_{5x} + k_y d_{1y} + \pi \frac{\Phi}{\Phi_0} \left( I - 1 + \frac{d_{5x}}{2d_{4x}} \right) \right) \\
 &\quad + \exp i \left( -k_x d_{5x} - k_y d_{1y} - \pi \frac{\Phi}{\Phi_0} \left( I - 1 + \frac{d_{5x}}{2d_{4x}} \right) \right),
 \end{aligned} \tag{2.37}$$

$$\begin{aligned}
 t''_{4,I=\text{even}} &= \exp i \left( k_x d_{5x} + k_y d_{1y} + \pi \frac{\Phi}{\Phi_0} \left( I - 1 + \frac{d_{2x}}{2d_{4x}} \right) \right) \\
 &\quad + \exp i \left( k_x d_{5x} - k_y d_{1y} - \pi \frac{\Phi}{\Phi_0} \left( I - 1 + \frac{d_{2x}}{2d_{4x}} \right) \right), \\
 tt''_{4,I=\text{even}} &= \exp i \left( -k_x d_{5x} + k_y d_{1y} + \pi \frac{\Phi}{\Phi_0} \left( I - 1 - \frac{d_{2x}}{2d_{4x}} \right) \right) \\
 &\quad + \exp i \left( -k_x d_{5x} - k_y d_{1y} - \pi \frac{\Phi}{\Phi_0} \left( I - 1 - \frac{d_{2x}}{2d_{4x}} \right) \right),
 \end{aligned} \tag{2.38}$$

where  $I = 1, 2, 3, \dots, 4R_B$ . It should be noted that the magnetic Hamiltonian matrix elements are real numbers for the  $(k_x = 0, k_y)$  LL states, as revealed in layered graphenes.

## 2.5 MoS<sub>2</sub>

A MoS<sub>2</sub> monolayer, as shown in figures 2.4(a) and (b), is composed of three atomic layers. A single layer of molybdenum atoms is sandwiched by two sulfur layers, in which the former alone forms a 2D triangular lattice. Each Mo atom interacts with six neighboring Mo atoms, as well as six neighboring S atoms (three on the top/bottom layer). The outermost shells of the Mo atom are 4d orbitals and those of the S atom are 3p orbitals. According to the theoretical calculations [23–25], the low-lying energy bands are mainly determined by three ( $4d_{z^2}, 4d_{xy}, 4d_{x^2-y^2}$ ) orbitals of the molybdenum atoms, i.e. the valence and conduction bands nearest to the chemical potential are predominantly contributed to from such orbitals. In contrast, energy bands dominated by the ( $4d_{xz}, 4d_{yz}$ ) orbitals of molybdenum, and the ( $3p_x, 3p_y, 3p_z$ ) orbitals of sulfide, as well as other inner orbitals, belong to the higher/deeper electronic states, so that these orbitals hardly affect the magnetic quantization.

Without applying a magnetic field, a unit cell of parallelogram (blue dashed curves) contains one Mo atom with six nearest-neighbor interactions. The

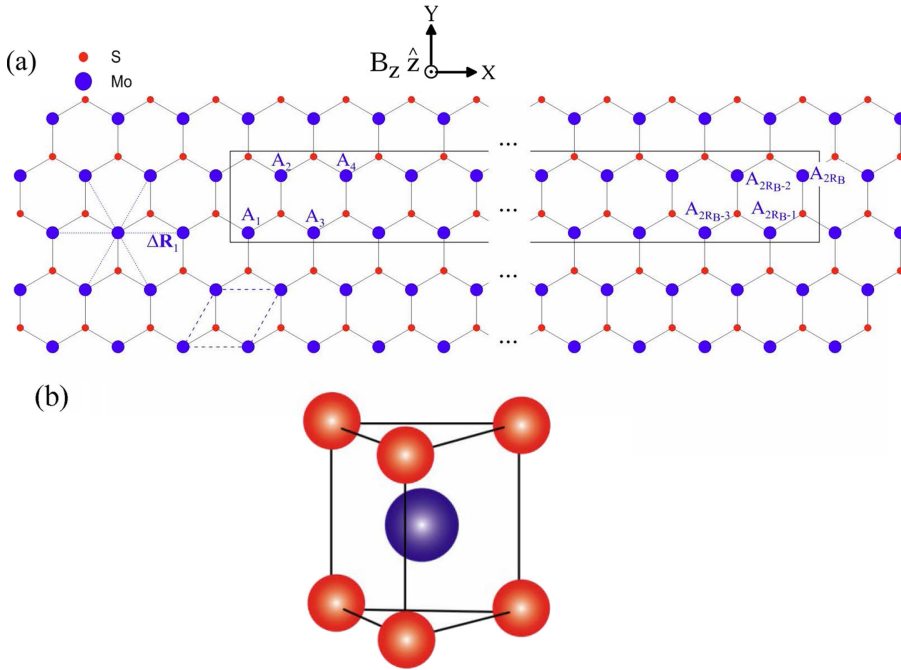


**Figure 2.4.** (a) Geometric structures for a MoS<sub>2</sub> monolayer with an enlarged rectangular unit cell in  $B_z \hat{z}$  and (b) the structure of trigonal prismatic coordination.



independent Hamiltonian matrix elements, which are built from the three tight-binding functions of  $(4d_{z^2}, 4d_{xy}, 4d_{x^2-y^2})$  orbitals, present the analytic form

$$\begin{aligned}
 \langle 4d_{z^2} | H | 4d_{z^2} \rangle &= 2\gamma_{11}(\cos 2\alpha'' + 2 \cos \alpha'' \cos \alpha''') + E_{o1}, \\
 \langle 4d_{z^2} | H | 4d_{xy} \rangle &= -2\sqrt{3}\gamma_{13} \sin \alpha'' \sin \alpha''' \\
 &\quad + 2i\gamma_{12}(\sin 2\alpha'' + \sin \alpha'' \cos \alpha'''), \\
 \langle 4d_{z^2} | H | 4d_{x^2-y^2} \rangle &= 2\sqrt{3}\gamma_{12} \cos \alpha'' \sin \alpha''' \\
 &\quad + 2\gamma_{13}(\cos 2\alpha'' - \cos \alpha'' \cos \alpha'''), \\
 \langle 4d_{xy} | H | 4d_{xy} \rangle &= 2\gamma_{22} \cos 2\alpha'' + (\gamma_{22} + 3\gamma_{33})\cos \alpha'' \cos \alpha''' \\
 &\quad + E_{o2}, \\
 \langle 4d_{xy} | H | 4d_{x^2-y^2} \rangle &= \sqrt{3}(\gamma_{33} - \gamma_{22})\sin \alpha'' \sin \alpha''' \\
 &\quad + 4i\gamma_{23} \sin \alpha''(\cos \alpha'' - \cos \alpha'''), \\
 \langle 4d_{x^2-y^2} | H | 4d_{x^2-y^2} \rangle &= 2\gamma_{33} \cos 2\alpha'' + (3\gamma_{22} + \gamma_{33})\cos \alpha'' \cos \alpha''' + E_{o2},
 \end{aligned} \tag{2.39}$$

where  $\alpha'' = \frac{1}{2}k_x a$  and  $\alpha''' = \frac{\sqrt{3}}{2}k_y a$ .  $a = 3.19 \text{ \AA}$  is the lattice constant between two neighboring Mo atoms. The nearest-neighbor hopping integrals of atomic orbitals are chosen as  $\gamma_{11} = -0.184 \text{ eV}$  ( $\chi_{d_{z^2}}(\mathbf{r}_I), \chi_{d_{z^2}}(\mathbf{r}_I + \Delta\mathbf{R}_I)$ ),  $\gamma_{12} = 0.401 \text{ eV}$  ( $\chi_{d_{z^2}}(\mathbf{r}_I), \chi_{d_{xy}}(\mathbf{r}_I + \Delta\mathbf{R}_I)$ ),  $\gamma_{13} = 0.507 \text{ eV}$  ( $\chi_{d_{z^2}}(\mathbf{r}_I), \chi_{d_{x^2-y^2}}(\mathbf{r}_I + \Delta\mathbf{R}_I)$ ),  $\gamma_{22} = 0.218 \text{ eV}$  ( $\chi_{d_{xy}}(\mathbf{r}_I), \chi_{d_{xy}}(\mathbf{r}_I + \Delta\mathbf{R}_I)$ ),  $\gamma_{23} = 0.057 \text{ eV}$  ( $\chi_{d_{xy}}(\mathbf{r}_I), \chi_{d_{x^2-y^2}}(\mathbf{r}_I + \Delta\mathbf{R}_I)$ ), and  $\gamma_{33} = 0.388 \text{ eV}$  ( $\chi_{d_{x^2-y^2}}(\mathbf{r}_I), \chi_{d_{x^2-y^2}}(\mathbf{r}_I + \Delta\mathbf{R}_I)$ ), where  $\chi_{d_{z^2}}(\mathbf{r}_I)$ ,  $\chi_{d_{xy}}(\mathbf{r}_I)$  and  $\chi_{d_{x^2-y^2}}(\mathbf{r}_I)$  are the atomic orbitals centered at  $\mathbf{r}_I$  [26]. The on-site energy is  $E_{o1} = 1.046 \text{ eV}$  added to the  $|4d_{z^2}\rangle$  orbital and  $E_{o2} = 2.104 \text{ eV}$  added to the  $|4d_{xy}\rangle$  and  $|4d_{x^2-y^2}\rangle$  orbitals.

Considering the spin degree of freedom, the number of the basis is doubled as  $\{|4d_{z^2}, \uparrow\rangle, |4d_{xy}, \uparrow\rangle, |4d_{x^2-y^2}, \uparrow\rangle, |4d_{z^2}, \downarrow\rangle, |4d_{xy}, \downarrow\rangle, |4d_{x^2-y^2}, \downarrow\rangle\}$ . The intra-atomic SOC interaction,  $V_{\text{SOC}} = \frac{\lambda_{\text{SOC}}}{2} L_z S_z$ , is expressed as

$$V_{\text{SOC}} = \begin{bmatrix} 0 & 0 & 0 & 0 & 0 & 0 \\ 0 & 0 & 2i & 0 & 0 & 0 \\ 0 & -2i & 0 & 0 & 0 & 0 \\ 0 & 0 & 0 & 0 & 0 & 0 \\ 0 & 0 & 0 & 0 & 0 & -2i \\ 0 & 0 & 0 & 0 & 2i & 0 \end{bmatrix}, \tag{2.40}$$

and the SOC coupling strength  $\lambda_{\text{SOC}} = 0.073 \text{ eV}$  [26]. Since the  $4d_{z^2}$  and the composite orbitals of  $\frac{1}{\sqrt{2}}(4d_{x^2-y^2} \pm 4d_{xy})$  correspond to the magnetic quantum numbers of 0 and  $\pm 2$ , respectively, the SOC interactions occur between the  $4d_{xy}$  and  $4d_{x^2-y^2}$  orbital electrons with the same spin orientation. In sharp contrast with tinene (equation (2.27)), the SOC interactions related to  $\lambda_{\text{SOC}}(\frac{L_+ S_- + L_- S_+}{2})$  are absent in  $\text{MoS}_2$ . The main reason is that  $L_{\pm}$  can only result in the coupling of two orbitals with the  $\pm 1$  difference in the magnetic quantum number.

Under the influence of  $B_z \hat{z}$  with  $\mathbf{A} = (0, B_z x, 0)$ , the unit cell becomes an enlarged rectangle containing  $2R_B$  Mo atoms (figure 2.4(a)). Consequently, the wave function is the linear combination of  $12R_B$  tight-binding functions  $\{|o_{Im}\rangle, I = 1, 2, \dots, 2R_B; o = 4d_{z^2}, 4d_{xy}, 4d_{x^2-y^2}; m = \uparrow, \downarrow\}$ . The nonzero and independent matrix elements of the magnetic Hamiltonian, which belong to the complex numbers even at  $k_x = 0$  and  $k_y = 0$ , are given by

$$\begin{aligned}
 \langle 4d_{z^2,I}|H|4d_{z^2,J}\rangle &= \gamma_{11} \exp(i2\alpha'')\delta_{J,I-2} + 2\gamma_{11} \cos \beta_J \exp(i\alpha'')\delta_{J,I-1} \\
 &\quad + \gamma_{11} \exp(-i2\alpha'')\delta_{J,I+2} \\
 &\quad + 2\gamma_{11} \cos \beta_{J-1} \exp(-i\alpha'')\delta_{J,I+1} + E_{o1}\delta_{J,I}, \\
 \langle 4d_{z^2,I}|H|4d_{xy,J}\rangle &= \gamma_{12} \exp(i2\alpha'')\delta_{J,I-2} \\
 &\quad + [\gamma_{12} \cos \beta_J + \sqrt{3} i\gamma_{13} \sin \beta_J] \exp(i\alpha'')\delta_{J,I-1} \\
 &\quad - \gamma_{12} \exp(-i2\alpha'')\delta_{J,I+2} + [-\gamma_{12} \cos \beta_{J-1} \\
 &\quad - \sqrt{3} i\gamma_{13} \sin \beta_{J-1}] \exp(-i\alpha'')\delta_{J,I+1}, \\
 \langle 4d_{z^2,I}|H|4d_{x^2-y^2,J}\rangle &= \gamma_{13} \exp(i2\alpha'')\delta_{J,I-2} \\
 &\quad + [-\gamma_{13} \cos \beta_J + \sqrt{3} i\gamma_{12} \sin \beta_J] \exp(i\alpha'')\delta_{J,I-1} \\
 &\quad + \gamma_{13} \exp(-i2\alpha'')\delta_{J,I+2} + [-\gamma_{13} \cos \beta_{J-1} \\
 &\quad + \sqrt{3} i\gamma_{12} \sin \beta_{J-1}] \exp(-i\alpha'')\delta_{J,I+1}, \\
 \langle 4d_{xy,I}|H|4d_{xy,J}\rangle &= \gamma_{22} \exp(i2\alpha'')\delta_{J,I-2} \\
 &\quad + \left[ \frac{1}{2}(\gamma_{22} + 3\gamma_{33})\cos \beta_J \right] \exp(i\alpha'')\delta_{J,I-1} \\
 &\quad + \gamma_{22} \exp(-i2\alpha'')\delta_{J,I+2} + \left[ \frac{1}{2}(\gamma_{22} + 3\gamma_{33})\cos \beta_{J-1} \right] \exp(-i\alpha'')\delta_{J,I+1} \\
 &\quad + E_{o2}\delta_{J,I}, \\
 \langle 4d_{x^2-y^2,I}|H|4d_{x^2-y^2,J}\rangle &= \gamma_{33} \exp(i2\alpha'')\delta_{J,I-2} \\
 &\quad + \left[ \frac{1}{2}(3\gamma_{22} + \gamma_{33})\cos \beta_J \right] \exp(i\alpha'')\delta_{J,I-1} \\
 &\quad + \gamma_{33} \exp(-i2\alpha'')\delta_{J,I+2} + \left[ \frac{1}{2}(3\gamma_{22} + \gamma_{33})\cos \beta_{J-1} \right] \exp(-i\alpha'')\delta_{J,I+1} \\
 &\quad + E_{o2}\delta_{J,I}, \\
 \langle 4d_{xy,I}|H|4d_{x^2-y^2,J}\rangle &= \gamma_{23} \exp(i2\alpha'')\delta_{J,I-2} - \gamma_{23} \exp(-i2\alpha'')\delta_{J,I+2} \\
 &\quad + \left[ -i\frac{\sqrt{3}}{2}(\gamma_{33} - \gamma_{22})\sin \beta_J - 2\gamma_{23} \cos \beta_J \right] \exp(i\alpha'')\delta_{J,I-1} \\
 &\quad + \left[ i\frac{\sqrt{3}}{2}(\gamma_{33} - \gamma_{22})\sin \beta_{J-1} + 2\gamma_{23} \cos \beta_{J-1} \right] \exp(-i\alpha'')\delta_{J,I+1},
 \end{aligned} \tag{2.41}$$

where  $\cos \beta_J = \cos[\alpha''' + \pi \frac{\Phi}{\Phi_0}(J + \frac{1}{2})]$  and  $\sin \beta_J = \sin[\alpha''' + \pi \frac{\Phi}{\Phi_0}(J + \frac{1}{2})]$ .

## 2.6 A suitable, reliable and wide-range model

The important characteristics of the generalized tight-binding model are worthy of a more detailed discussion. This model can fully comprehend the essential electronic properties under various external fields, compared with the effective-mass model. It is suitable for the uniform/modulated electric fields [27], uniform/modulated magnetic fields [28] (details in chapter 7), and the composite fields [29], since all the intrinsic interactions and the external fields are included in the calculations of band structures and wave functions simultaneously. Moreover, the dependences on the distinct sublattices, the multi- and single-orbital hybridizations and spin arrangements are explored in detail (discussed later in chapters 3–6). Such factors are responsible for the main features of the physical properties, e.g. the diverse and complicated LL anti-crossing spectra. However, the low-energy perturbation about the high symmetry points is first made on the Hamiltonian matrix elements and then the magnetic quantization is done. Such an approximation cannot accurately deal with the quantized states closely related to the partially flat, sombrero-shaped and multi-valley energy bands, as discussed above for the tetra-layer ABC-stacked graphene, monolayer tinene, and bilayer phosphorene. Evidently, further studies on the LL-induced fundamental properties will become cumbersome. For example, it is difficult to understand the magneto-optical properties and Coulomb excitations using the effective-mass model.

The generalized tight-binding model could also be used to investigate the essential physical properties of condensed-matter systems with any dimensions (details in chapter 7), e.g. various carbon-related systems. Systematic studies on the rich and unique magnetic quantization have been made for three kinds of bulk graphites (simple hexagonal, Bernal and rhombohedral graphites) [30–32], layered graphenes [33–36], 1D carbon nanotube [31], and graphene nanoribbons [38, 39]. They clearly show that a very strong competition or cooperation between the geometric structure and magnetic field can create an unusual quantization phenomenon, i.e. the magnetic quantization is greatly diversified by the different dimensions, stacking configurations, and boundary conditions. The dimensional crossover, corresponding to the dramatic changes of essential properties, is expected to be revealed in other emergent materials, e.g. layered phosphorenes and bulk phosphorous.

The calculated results are reliable at low and middle energies. The layer-, sublattice-, orbital- and spin-dependent energy spectra and wave functions can account for the other essential physical properties (chapter 7), such as quantum transport properties, optical spectra and Coulomb excitations. The generalized tight-binding model could combine with the single- and many-particle theories, when the latter are expressed in layer-dominated forms. For example, the random-phase approximation (RPA), which can evaluate the effective electron–electron Coulomb interactions, needs to be transformed to obtain the layer-dominated response function [15, 16]. Up to now, theoretical studies cover optical properties [16, 17, 19, 21–23] and electronic excitations [15–19, 26, 27] of layered graphenes under electric and magnetic fields. In particular, the optical selection rules of the available transition channels and the phase diagrams of the dynamic Coulomb screenings are obtained from the main

features of electronic properties. In short, the generalized tight-binding model can solve the various Hamiltonians efficiently and thus is very useful in understanding the essential physical properties of condensed-mater systems.

## 2.7 Numerical calculations

In this section, we introduce the generalized tight-binding model, which has been adapted to deal with different interactions in emergent 2D materials and to obtain the corresponding Hamiltonian matrices. The eigenvalues and eigenfunctions can be obtained by diagonalizing the Hamiltonian matrix. To gain an understanding of the electronic properties, the band structure in the first Brillouin zone is required; a proposition that implies the diagonalization of Hamiltonian matrices for thousands of different  $k$ 's. In the presence of  $\mathbf{B}_z$ , the first Brillouin zone is greatly reduced, but the deduced magnetic Hamiltonian matrix is huge and difficult to be diagonalized. These problems can be solved by means of numerical calculations. We take monolayer graphene as an example to explain the numerical calculation process. At  $B_z = 0$ , there are two carbon atoms in a unit cell and the interaction between  $2p_z$  orbitals of carbon atoms is considered. The  $2 \times 2$  Hamiltonian matrix is expressed as

$$\begin{bmatrix} 0 & \langle A_{\mathbf{k}} | H | B_{\mathbf{k}} \rangle \\ \langle A_{\mathbf{k}} | H | B_{\mathbf{k}} \rangle^* & 0 \end{bmatrix}. \quad (2.42)$$

The  $k$ -dependent matrix elements may be obtained from equation (2.2). The Hermitian matrix can be numerically solved by using numerical libraries such as IMSL and LAPACK. The application of  $\mathbf{B}_z$  enlarges the unit cell and the magnetic Hamiltonian matrix. In the bases  $|A_{1\mathbf{k}}\rangle$ ,  $|B_{1\mathbf{k}}\rangle$ ,  $|A_{2\mathbf{k}}\rangle$ ,  $|B_{2\mathbf{k}}\rangle$ , ...,  $|A_{2R_B-1\mathbf{k}}\rangle$ ,  $|B_{2R_B-1\mathbf{k}}\rangle$ ,  $|A_{2R_B\mathbf{k}}\rangle$ ,  $|B_{2R_B\mathbf{k}}\rangle$ , the  $4R_B \times 4R_B$  Hamiltonian matrix is

$$\begin{bmatrix} 0 & p_1 & 0 & 0 & \cdots & 0 & 0 & t_3 \\ p_1^* & 0 & t_3 & 0 & \cdots & 0 & 0 & 0 \\ 0 & t_3^* & 0 & p_2 & \cdots & 0 & 0 & 0 \\ 0 & 0 & p_2^* & 0 & t_3 & \cdots & 0 & 0 \\ \vdots & \vdots & \vdots & t_3^* & \vdots & \cdots & \vdots & \vdots \\ 0 & 0 & 0 & \vdots & \cdots & \vdots & t_3 & 0 \\ 0 & 0 & 0 & 0 & \cdots & t_3^* & 0 & p_{2R_B} \\ t_3^* & 0 & 0 & 0 & \cdots & 0 & p_{2R_B}^* & 0 \end{bmatrix}. \quad (2.43)$$

In this notation,  $p_I$  is defined as  $t_{1,I} + t_{2,I}$  and the elements of the magnetic Hamiltonian matrix are determined by equations (2.4) and (2.5). For small  $B_z$ , diagonalizing a  $4R_B \times 4R_B$  Hamiltonian matrix is a difficult task ( $R_B \sim 7900$  at  $B_z = 10$  T). It is very time-consuming even on a high-performance computer with a considerable amount of physical memory. Fortunately, this problem can be simplified by rearranging the bases. In the bases  $|A_{1\mathbf{k}}\rangle$ ,  $|B_{2R_B\mathbf{k}}\rangle$ ,  $|B_{1\mathbf{k}}\rangle$ ,  $|A_{2R_B\mathbf{k}}\rangle$ ,  $|A_{2\mathbf{k}}\rangle$ ,  $|B_{2R_B-1\mathbf{k}}\rangle$ ,  $|B_{2\mathbf{k}}\rangle$ ,  $|A_{2R_B-1\mathbf{k}}\rangle$ ..., the  $4R_B \times 4R_B$  Hamiltonian matrix is expressed as

$$\begin{bmatrix}
0 & t_3^* & p_1 & 0 & \cdots & 0 & 0 & 0 \\
t_3 & 0 & 0 & p_{2R_B}^* & \cdots & 0 & 0 & 0 \\
p_1^* & 0 & 0 & 0 & t_3 & \cdots & 0 & 0 \\
0 & p_{2R_B} & \vdots & 0 & \cdots & \ddots & \vdots & 0 \\
\vdots & \vdots & t_3^* & \vdots & \vdots & \vdots & p_{R_B} & \vdots \\
0 & 0 & 0 & \ddots & \cdots & 0 & 0 & p_{R_B+1}^* \\
0 & 0 & 0 & \cdots & p_{R_B}^* & 0 & 0 & t_3^* \\
0 & 0 & 0 & 0 & \cdots & p_{R_B+1} & t_3 & 0
\end{bmatrix}. \quad (2.44)$$

This Hermitian matrix with an upper band width of two can be stored as a  $4R_B \times 3$  band matrix. Using the library routine to solve the band matrix would substantially reduce the calculation time. The dispersionless energy spectrum means that a  $k$  state is sufficient to describe the energy spectrum of the first Brillouin zone. In addition, all of the matrix elements become real numbers at  $(k_x = 0, k_y = 0)$ , which can further reduce the calculation time. This numerical characteristic also applies to monolayer and bilayer phosphorenes and layered graphenes with normal stacking configurations. For silicene, germanene, tinene and  $\text{MoS}_2$ , the numerical calculation process is similar but the multi-orbital bonding and spin degree of freedom result in the enlargement of the Hamiltonian matrix. It should be noted that their Hamiltonian matrices are complex for all  $k$ 's, leading to a longer calculation time.

A numerical calculation within the framework of the generalized tight-binding model enables us to thoroughly investigate the electronic properties of materials. The characteristics of electronic structures and wave functions are well depicted. Moreover, the results are accurate and reliable within a wide energy range. In this book, the energy bands along the high-symmetry directions are plotted to illustrate the main features of the electronic structure of the emergent 2D materials. The orbital decomposed state probabilities at the high-symmetry points can reveal the dominant atomic orbital of each energy. The zero-field band structure determines the main characteristics of the quantized LL states, such as the sublattice dominance in the Landau states, the field-dependent LL energies and the inter- and intra-group LL anticrossings. In the presence of  $B_z$ , the length of the enlarged unit cell is obviously greater than the magnetic length. Thus, the localized subenvelope function which is the combination of the  $2R_B$  tight-binding functions exhibits a sequential spatial distribution in the enlarged unit cell. Well behaved in spatial distributions, the subenvelope functions with a normal zero-point number and a spatial symmetry/antisymmetry at the localization center can characterize the quantum numbers of the LLs.

## References

- [1] Charlier J-C, Michenaud J-P and Gonze X 1992 First-principles study of the electronic properties of simple hexagonal graphite *Phys. Rev. B* **46** 4531

- [2] Do T N, Chang C P, Shih P H and Lin M F 2017 Stacking-enriched magnetotransport properties of few-layer graphenes *Phys. Chem. Chem. Phys.* **19** 29525
- [3] Ho Y H, Chiu C W, Su W P and Lin M F 2014 Magneto-optical spectra of transition metal dichalcogenides: a comparative study *Appl. Phys. Lett.* **105** 222411
- [4] Ho Y H, Wang Y H and Chen H Y 2014 Magneto-electronic and optical properties of a MoS<sub>2</sub> monolayer *Phys. Rev. B* **89** 55316
- [5] Huang Y C, Chang C P and Lin M F 2008 Magnetoabsorption spectra of bilayer graphene ribbons with Bernal stacking *Phys. Rev. B* **78** 115422
- [6] Lin Y P, Lin C Y, Ho Y H, Do T N and Lin M F 2015 Magneto-optical properties of ABC-stacked trilayer graphene *Phys. Chem. Chem. Phys.* **17** 15921–7
- [7] Chen R B, Chiu Y H and Lin M F 2014 Beating oscillations of magneto-optical spectra in simple hexagonal graphite *Comput. Phys. Commun.* **189** 60–5
- [8] Chen R B, Chiu Y H and Lin M F 2012 A theoretical evaluation of the magneto-optical properties of AA-stacked graphite *Carbon* **54** 268–76
- [9] Ho Y H, Chiu Y H, Lin D H, Chang C P and Lin M F 2010 Magneto-optical selection rules in bilayer Bernal graphene *ACS Nano* **4** 1465–72
- [10] Wu J Y, Lin C Y, Gumbs G and Lin M F 2015 The effect of perpendicular electric field on temperature-induced plasmon excitations for intrinsic silicene *RSC Adv.* **5** 51912–8
- [11] Wu J Y, Chen S C and Lin M F 2014 Temperature-dependent Coulomb excitations in silicene *New J. Phys.* **16** 125002
- [12] Wu J Y, Chen S C, Gumbs G and Lin M F 2016 Feature-rich electronic excitations in external fields of 2D silicene *Phys. Rev. B* **94** 205427
- [13] Wu J Y, Gumbs G and Lin M F 2014 Combined effect of stacking and magnetic field on plasmon excitations in bilayer graphene *Phys. Rev. B* **89** 165407
- [14] Wu J Y, Chen S C, Roslyak O, Gumbs G and Lin M F 2011 Plasma excitations in graphene: Their spectral intensity and temperature dependence in magnetic field *ACS Nano* **5** 1026–32
- [15] Ho Y H, Chang C P and Lin M F 2006 Electronic excitations of the multilayered graphite *Phys. Lett. A* **352** 446–50
- [16] Ho Y H, Lu C L, Hwang C C, Chang C P and Lin M F 2006 Coulomb excitations in AA- and AB-stacked bilayer graphites *Phys. Rev. B* **74** 085406
- [17] Lin M F, Chuang Y C and Wu J Y 2012 Electrically tunable plasma excitations in AA-stacked multilayer graphene *Phys. Rev. B* **86** 125434
- [18] Chuang Y C, Wu J Y and Lin M F 2013 Electric field dependence of excitation spectra in AB-stacked bilayer graphene *Sci. Rep.* **3** 1368
- [19] Chuang Y C, Wu J Y and Lin M F 2013 Electric-field-induced plasmon in AA-stacked bilayer graphene *Ann. Phys.* **339** 298–306
- [20] Charlier J C and Michenaud J P 1992 Tight-binding density of electronic states of pregraphitic carbon *Phys. Rev. B* **46** 4540
- [21] Chadi D J 1977 Spin-orbit splitting in crystalline and compositionally disordered semiconductors *Phys. Rev. B* **16** 790
- [22] Cardona M, Shaklee K L and Pollak F H 1967 Electroreflectance at a semiconductor-electrolyte interface *Phys. Rev.* **154** 696
- [23] Zhu Z Y, Cheng Y C and Schwingenschlögl U 2011 Giant spin-orbit-induced spin splitting in two-dimensional transition-metal dichalcogenide semiconductors *Phys. Rev. B* **84** 153402
- [24] Lebègue S and Eriksson O 2009 Electronic structure of two-dimensional crystals from *ab initio* theory *Phys. Rev. B* **79** 11409

- [25] Ataca C and Ciraci S 2011 Functionalization of single-layer MoS<sub>2</sub> honeycomb structures *J. Phys. Chem. C* **115** 13303
- [26] Liu G-B, Shan W-Y, Yao Y, Yao W and Xiao D 2013 Three-band tight-binding model for monolayers of group-VIB transition metal dichalcogenides *Phys. Rev. B* **88** 085433
- [27] Ou Y C, Chiu Y H, Lu J M, Su W P and Lin M F 2013 Electric modulation effect on magneto-optical spectrum of monolayer graphene *Comput. Phys. Commun.* **184** 1821–6
- [28] Ou Y C, Sheu J K, Chiu Y H, Chen R B and Lin M F 2011 Influence of modulated fields on the Landau level properties of graphene *Phys. Rev. B* **83** 195405
- [29] Ou Y C, Chiu Y H, Yang P H and Lin M F 2014 The selection rule of graphene in a composite magnetic field *Opt. Express* **22** 7473
- [30] Ho Y H, Wang J, Chiu Y H, Lin M F and Su W P 2011 Characterization of Landau subbands in graphite: A tight-binding study *Phys. Rev. B* **83** 121201
- [31] Ho C H, Chang C P and Lin M F 2014 Landau subband wave functions and chirality manifestation in rhombohedral graphite *Solid State Commun.* **197** 11–5
- [32] Chen R B and Chiu Y H 2013 Landau subband and Landau level properties of AA-stacked graphene superlattice *J. Nanosci. Nanotechnol.* **12** 2557–66
- [33] Huang Y K, Chen S C, Ho Y H, Lin C Y and Lin M F 2014 Feature-rich magnetic quantization in sliding bilayer graphenes *Sci. Rep.* **4** 7509
- [34] Lin C Y, Wu J Y, Chiu Y H and Lin M F 2014 Stacking-dependent magneto-electronic properties in multilayer graphenes *Phys. Rev. B* **90** 205434
- [35] Lai Y H, Ho J H, Chang C P and Lin M F 2008 Magnetoelectronic properties of bilayer Bernal graphene *Phys. Rev. B* **77** 085426
- [36] Lin C Y, Wu J Y, Ou Y J, Chiu Y H and Lin M F 2015 Magneto-electronic properties of multilayer graphenes *Phys. Chem. Chem. Phys.* **17** 26008–35
- [37] Shyu F L, Chang C P, Chen R B, Chiu C W and Lin M F 2003 Magnetoelectronic and optical properties of carbon nanotubes *Phys. Rev. B* **67** 045405
- [38] Huang Y C, Lin M F and Chang C P 2008 Landau levels and magneto-optical properties of graphene ribbons *J. Appl. Phys.* **103** 073709
- [39] Huang Y C, Chang C P and Lin M F 2007 Magnetic and quantum confinement effects on electronic and optical properties of graphene ribbons *Nanotechnology* **18** 495401